





Enhanced plasma performance in C-2W advanced beam-driven field-reversed configuration experiments

H. Gota^{1,*} , A. Smirnov¹, M.W. Binderbauer¹ , T. Tajima^{1,2}, S. Putvinski¹, J.B. Titus¹ , M. Nations¹ , T. Roche¹ , E. Trask¹ , T. DeHaas¹ , S.A. Dettrick¹ , E.M. Granstedt¹ , D.K. Gupta¹ , S. Gupta¹ , A.A. Ivanov¹, S. Korepanov¹ , R.M. Magee¹ , T. Matsumoto¹ , J.A. Romero¹ , P. Yushmanov¹, K. Zhai¹ , L. Schmitz^{1,3} , Z. Lin² , S. Krasheninnikov⁴ , E.A. Baltz⁵ , J.C. Platt⁵ , E.V. Belova⁶ , T. Asai⁷ , A.I. Smolyakov⁸ , S. Abdollahi¹, S. Abramov¹, A. Alexander¹, I. Allfrey¹ , R. Andow¹, D.C. Barnes¹, B. Barnett¹, J. Barrett¹ , M. Beall¹ , N.G. Bolte¹ , E. Bomgardner¹, A. Bondarenko¹ , F. Brighenti¹, J. Buttery¹, S. Caton¹, F. Ceccherini¹ , Y. Choi¹, R. Clary¹ , A. Cooper¹, C. Deng¹ , A. de Vera¹, J. Drobny¹, A. Dunaevsky¹, C. Exton¹, A. Fareed¹ , P. Feng¹, C. Finucane¹, D. Fluegge¹, A. Fontanilla¹, Y. Fujiwara¹, L. Galeotti¹ , S. Galkin¹ , R. Groenewald¹ , T. Hsyu¹, K. Hubbard¹, R. Jaber¹ , L. Jian¹, N. Kafle¹ , S. Kamio^{1,2} , S. Karbasheski¹ , J.S. Kinley¹, A. Korepanov¹, G. Koumarianou¹ , S. Krause¹ , P. Kudrin¹, C.K. Lau¹ , H. Leinweber¹, J. Leuenberger¹, D. Lieurance¹, M. Litton¹ , R. Luna¹, R. Luong¹, J. MacFarlane¹ , D. Madura¹, J. Margo¹, D. Marshall¹ , V. Matvienko¹, M. Meekins¹, W. Melian¹, R. Mendoza¹ , R. Michel¹, M. Morehouse¹, Y. Musthafa¹, S. Nazarenko¹, A. Necas¹, B.S. Nicks¹ , N. Nwoke¹, S. Ohshima^{1,2} , M. Onofri¹ , R. Page¹, J. Park¹, E. Parke¹ , S. Patel¹ , L. Pennings¹, K. Phung¹ , G. Player^{1,2} , L. Rios¹, I. Sato¹, J.H. Schroeder¹, Y. Shimabukuro^{1,2}, M. Showers¹, A. Sibley¹, M. Signorelli¹, M. Slepchenkov¹, R.J. Smith¹ , G. Snitchler¹, V. Sokolov¹ , D. Solyakov¹, Y. Song¹, B. Sporer¹ , L.C. Steinhauer¹ , C. Stonier¹ , A. Stratta^{1,2}, J. Sweeney¹, M. Tobin¹ , M. Tuszewski¹, J. Ufnal¹, T. Valentine¹, S. Vargas¹, A.D. Van Drie¹ , V. Vekselman¹, A. Veksler¹ , C. Weixel¹, C. White¹, M. Wollenberg¹, J. Wood¹ , Y. Zhou¹ , S. Ziaei¹ and the TAE Team¹

¹ TAE Technologies, Inc., Foothill Ranch, CA, United States of America

² University of California at Irvine, Irvine, CA, United States of America

³ University of California at Los Angeles, Los Angeles, CA, United States of America

⁴ University of California at San Diego, San Diego, CA, United States of America

⁵ Google LLC, Mountain View, CA, United States of America

⁶ Princeton Plasma Physics Laboratory, Princeton, NJ, United States of America

⁷ Nihon University, Tokyo, Japan

⁸ University of Saskatchewan, Saskatoon, Saskatchewan, Canada

* Author to whom any correspondence should be addressed.



Original content from this work may be used under the terms of the [Creative Commons Attribution 4.0 licence](https://creativecommons.org/licenses/by/4.0/). Any further distribution of this work must maintain attribution to the author(s) and the title of the work, journal citation and DOI.

E-mail: hgota@tae.com

Received 27 November 2023, revised 23 March 2024

Accepted for publication 29 April 2024

Published 23 August 2024



Abstract

TAE Technologies' fifth-generation fusion device, C-2W (also called 'Norman'), is the world's largest compact-toroid device and has made significant progress in field-reversed configuration (FRC) plasma performance. C-2W produces record breaking, macroscopically stable, high-temperature advanced beam-driven FRC plasmas, dominated by injected fast particles and sustained in steady state, which is primarily limited by neutral-beam (NB) pulse duration. The NB power supply system has recently been upgraded to extend the pulse length from 30 ms to 40 ms, which allows for a longer plasma lifetime and thus better characterization and further enhancement of FRC performance. An active plasma control system is routinely used in C-2W to produce consistent FRC performance as well as for reliable machine operations using magnet coils, edge-biasing electrodes, gas injection and tunable-energy NBs. Google's machine learning framework for experimental optimization has also been routinely used to enhance plasma performance. Dedicated plasma optimization experimental campaigns, particularly focused on the external magnetic field profile and NB injection (NBI) optimizations, have produced a superior FRC plasma performance; for instance, achieving a total plasma energy of ~ 13 kJ, a trapped poloidal magnetic flux of ~ 16 mWb (based on the rigid-rotor model) and plasma sustainment in steady state up to ~ 40 ms. Furthermore, under some operating conditions, the electron temperature of FRC plasmas at a quiescent phase has successfully reached up to ~ 1 keV at the peak inside the FRC separatrix for the first time. The overall FRC performance is well correlated with the NB and edge-biasing systems, where higher total plasma energy is obtained with higher NBI power and applied voltage on biasing electrodes. C-2W operations have now reached a mature level where the machine can produce hot, stable, long-lived, and repeatable plasmas in a well-controlled manner.

Keywords: field-reversed configuration, compact toroid, neutral beam injection, aneutronic fusion, beam-driven FRC

(Some figures may appear in colour only in the online journal)

1. Introduction

TAE Technologies (TAE; formerly Tri Alpha Energy) was spun off from the University of California at Irvine and established in 1998 by the late Prof. Norman Rostoker as a fusion start-up private company, aiming for the development and steady operation of commercial fusion reactors. It is currently one of the world's largest privately funded fusion research and development companies. TAE's concept of a magnetically confined fusion reactor is based on utilizing a field-reversed configuration (FRC) [1, 2] as the core plasma and performing plasma heating and current drive primarily via high-energy and high-power neutral-beam (NB) injection (NBI). An FRC is a high-beta (the ratio of plasma pressure to external magnetic pressure; volume average beta $\langle \beta \rangle$ near unity) compact toroid (CT), consisting of a poloidal magnetic field inside closed-field lines with its separatrix surrounded by open-field lines. TAE's advanced beam-driven FRC produces an FRC-mirror hybrid plasma, predominantly composed of injected fast ions circulating inside and outside of the separatrix [3, 4]. TAE's approach is to eventually adopt advanced fuels such as hydrogen-boron ($p\text{-}^{11}\text{B}$) with the ultimate aim of a safe

and economical fusion reactor that does not generate neutrons in its primary fusion reaction [5, 6]. This approach also has many technological advantages and it is relatively compact and easy to design, construct, and operate the fusion reactor because concerns about neutron-induced damage to the reactor are vastly reduced.

TAE's current experimental device, C-2W (also called 'Norman', shown in figure 1), is the company's fifth-generation FRC machine and the world's largest CT device, producing high-magnetic-flux, high-temperature, macroscopically stable, long-lived FRC plasmas [4, 7]. In the preceding C-2 [8, 9] and C-2U [10, 11] experiments, the main goals were to demonstrate reliable and stable FRC formation and sustainment of the FRC by NBI and edge biasing (i.e. aiming for a 'long enough' milestone) [12, 13], and the present C-2W experiment has been primarily focused on producing a high-temperature FRC regime (i.e. aiming for a 'hot enough' milestone; designed goal of total plasma temperature $T_{\text{tot}} \geq 3$ keV) to verify the previously emerged TAE's energy scaling law [11, 14].

As previously reported in [4], C-2W has successfully produced high-temperature FRC plasmas via high-energy and

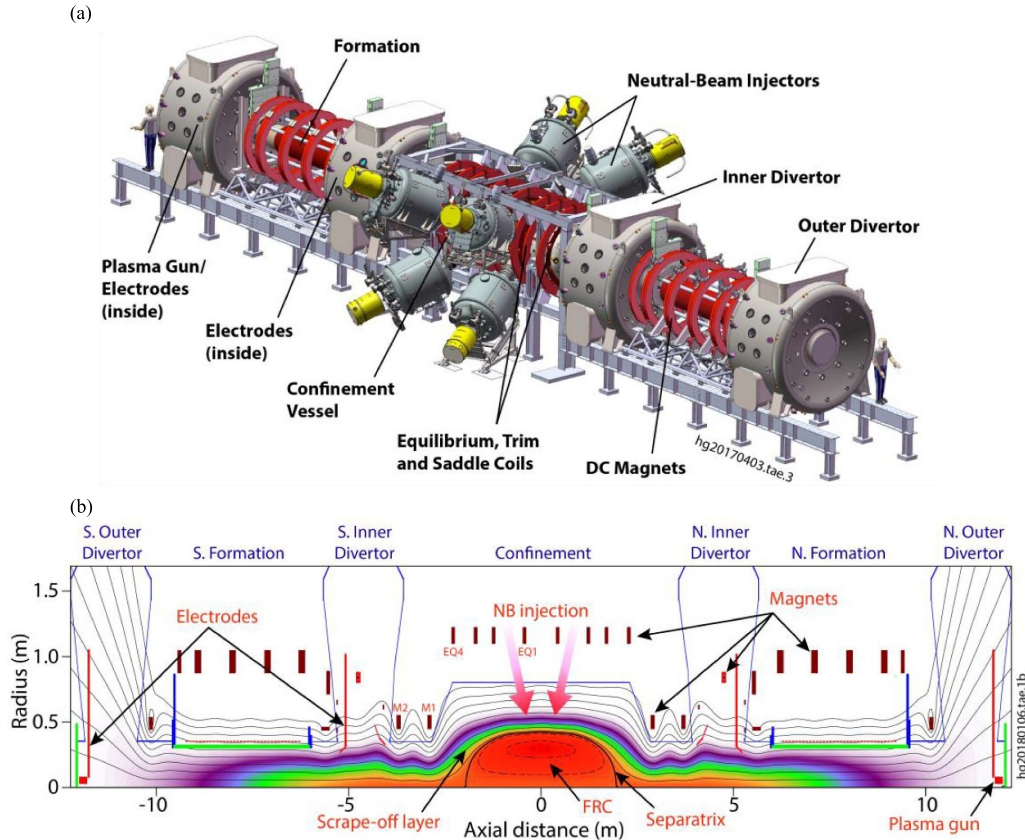


Figure 1. (a) Illustration of TAE’s fifth-generation experimental device, C-2W (a.k.a. Norman), consisting of the central confinement section surrounded by two inner divertors, two formation sections, and two outer divertors. Eight NB injectors (four of 15 keV fixed-energy NBs, and the other four of 15–40 keV tunable-energy NBs) are installed in the central region of the confinement vessel. Plasma guns and electrodes are mounted inside divertors. (b) Sketch of FRC magnetic topology and density contours, calculated by 2D multi-fluid force-balanced equilibrium code, where field-line contours are traced and plasma densities are indicated with colors (red–purple color gradient indicates high–low densities).

high-power NBI, sustained in steady state until the end of the NBI pulse duration. After the achievement of the ‘hot enough’ milestone, we have re-focused the C-2W fusion program to support the development of our sixth-generation fusion device, called ‘Copernicus.’ Basically, C-2W has become an ideal test-bed for Copernicus, and is now being used to test proposed new experimental concepts for Copernicus in order to mitigate the risk inherent in building a next-step device. The new C-2W research focus and activities include (but are not limited to) the following: further improving plasma performance by upgrading and optimizing the NBI system and its operations [15]; demonstrating and mastering real-time plasma feedback control [16, 17]; optimizing the edge-biasing scheme with various electrode-biasing configurations and operations [18, 19] as well as testing different electrode geometries and materials; further optimizing the external magnetic fields throughout the machine, including different configurations of confinement mirror magnets and magnetic mirror plugs [20]; and optimizing gas/particle fueling and its control systems, including a new insertable fueling pipe to inject gas at a desired radial location.

This paper briefly reviews the C-2W experimental apparatus, including recent machine/subsystem modifications and upgrades, in section 2. Recent FRC plasma performance

enhancement through various system optimizations such as on magnetic field profile, NBI power and beam impact parameter, and electrode biasing is described in section 3. Finally, the paper is summarized in section 4.

2. C-2W experimental apparatus

The C-2W experimental device, shown in figure 1(a), is the world’s largest theta-pinch CT collisional-merging system, and utilizes a high-power NBI and edge-biasing system to form and sustain FRC plasmas. Figure 1(b) illustrates the typical FRC and open-field-line magnetic topology as well as the density contours in C-2W, obtained from a 2D multi-fluid force-balanced equilibrium calculation using the LReqMI code [21], where field-line contours are traced and plasma densities are indicated with colors (red–purple gradient indicates high–low densities). The C-2W device is about 30 m long in overall length and consists of seven distinct sections: the central confinement section, surrounded by two inner divertors, two theta-pinch formation sections, and two outer divertors. The central confinement vessel (CV) is made of Inconel and has an inner-wall radius $r_w \sim 0.8$ m with a thin wall (resistive wall time < 5 ms), allowing for an external

magnetic-field ramp-up during a plasma discharge as required. Because of the relatively short CV wall time, an adequately controlled external magnetic field is important and critical to FRC plasma confinement as well as for plasma ramp-up. The four divertor vessels are made of stainless steel and have a large internal volume to accommodate high-volumetric pumping during a plasma discharge; moreover, each divertor has its own internal cryogenic pumping system with titanium gettering and a liquid-nitrogen (LN₂) cooling system to enhance the pumping capability inside the divertors (nominal pumping speed up to $\sim 2 \times 10^6$ L s⁻¹ per divertor). The LN₂ cooling system plays important roles in not only keeping the titanium sticking coefficient high on the divertor wall, cryogenic box, and electrode surfaces but also in keeping the in-vessel temperature cold to manage heat load on internal components such as internal mirror plugs. The two cylindrical formation tubes are made of opaque quartz, whose dimensions are ~ 3.5 m in length and ~ 0.6 m in diameter. The overall C-2W device accommodates an ultra-high vacuum (typically in the range of high 10^{-10} to low 10^{-9} Torr) with adequately set up wall conditioning and pumping systems in the CV and divertors. The CV is also equipped with 10+ insertable titanium-gettering systems for effective wall conditioning before the start of a day of C-2W operations and even between plasma shots as desired.

The C-2W magnet systems consist of confinement equilibrium (EQ) and mirror (M) coils, saddle and trim coils in the confinement section, in-vacuum fast-switching coils inside the divertors, pulsed-power coil straps in the formation sections, DC formation and external divertor coils, and magnetic-mirror plug coils located at the entrance of outer divertors, where the overall coil configuration is symmetrically arranged relative to the machine mid-plane ($z = 0$). In the confinement section, as illustrated in figure 1(b), there are 12 main magnets arranged from the mid-plane as EQ1, EQ2, EQ3, EQ4, M1 and M2 on both north and south sides symmetrically. In the formation sections, there are 17 sets of independently controlled pulsed-power formation coils located just outside the quartz tube per side. The current waveforms of each EQ and M coil are independently controlled (in either feedforward or feedback mode), which allows for flexible control of the external magnetic field profile as well as the plasma shape and position. In a typical C-2W experiment, the external magnetic field, B_z , in the confinement section is about 0.1–0.13 T, which can be increased up to ~ 0.3 T as desired. Trim coils placed beneath each of the EQ coils can also be operated independently to correct error fields as well as to perform active feedback control using the real-time plasma control system (RTPCS) [16, 17]. There are two types of magnetic-mirror plug configurations tested in C-2W: initially, large-bore external mirror-plug coils that generate magnetic field up to ~ 1 T [4, 7] and lately upgraded to an internal (in-vacuum, small-bore) magnetic-mirror plug configuration that can produce stronger magnetic field up to ~ 3 T. This strong magnetic-mirror plug field allows for more flexibility and a wider operational range to control mirror ratio (the ratio of the mirror field to the central confinement magnetic field) and also field expansion in the divertor region.

Eight NB injectors are installed on the CV, four of which have a tunable beam energy (15–40 keV, ~ 140 A per beam line) capability [22] and the other four injectors have a fixed beam energy (15 keV, ~ 140 A each) [23]. Total NB input power (electrical power on the NB power supplies + neutralization efficiency) with all 15 keV NBs is ~ 13 MW and can be increased up to ~ 20 MW by ramping up beam energies. Generally, attenuated power is estimated to be less than half of the electrical power due to a menagerie of neutralization efficiency, duct geometry, impact ionization and charge-exchange effects; an example estimation can be found in [24]. The NB power supplies have recently been upgraded to extend the pulse length from 30 ms to 40 ms, which enables a longer plasma lifetime and thus better characterization and further enhancement of FRC performance. The NBI angle was originally fixed at 70° relative to the machine axis but recently changed to 57° for the four tunable-energy NBs to study the effects of variations in the source distribution [25]. The average NBI impact parameter is $b \sim 20$ cm (adjustable within ± 3 cm; co-current injection into the FRC) which enables sufficient coupling between the beams and the target FRC plasma (typical radius of ~ 40 – 45 cm). The NBs provide energetic particles with a large orbit size crossing inside and outside the FRC separatrix that stabilize global magnetohydrodynamic (MHD) modes. The high-power NBs also provide a significant amount of fast-ion population and pressure inside the core region, thus producing beam-driven FRC plasmas. During the plasma pressure build-up via ramping up the NBI power, the external magnetic field in the CV also needs to be increased to maintain the plasma radius (i.e. prevent the plasma from touching the CV wall). Furthermore, this external magnetic field increase and proper adjustment is important to manage the orbit size of injected high-energy fast ions, so as not to scrape the CV wall.

To electrically bias the open-field lines of the scrape-off layer (SOL) outside the FRC separatrix, a set of coaxial plasma guns and concentric annular electrodes is installed inside each outer divertor as illustrated in figure 1. The biasing electrode system [18] has a good flexibility in terms of its operation where relatively high voltage (up to ~ 5 kV) can be applied on the electrodes (with a choice of any desired connections to the high-voltage and grounding cables [19]) and its pulse duration can be set for longer than 40 ms (i.e. longer than the NB pulse duration). Electrical potentials on these electrodes can be controlled independently by its power supplies, where active voltage and current control has been implemented using the RTPCS and is now routinely used to monitor, control and maintain reliable edge-biasing current and potential. Together with proper magnetic field control and gas/density control in the CV and divertor regions, this electrode biasing current and voltage control is a key element of reliable C-2W operations, particularly for effective edge/boundary control of FRCs via open-field lines/SOL. The role of the SOL and divertors is not only to provide a favorable boundary condition for the core FRC plasma but also to handle energy and particle exhaust from the core. Some specific cases of electrode biasing for plasma rotation control as well as active control

on electrode biasing current and voltage are described in section 3.4 below.

The diagnostic configuration of C-2W comprises more than 75 operational systems with plans for further expansion [26, 27]. The major components of this suite are broken up into four main categories: probes and bolometers, spectroscopy and imaging, fast-ion detection, and lasers. There are certainly overlaps in these categories, but they segment the space through the following distinctions: direct particle and field measurements (magnetic probes, bolometers, energy analyzers, etc), plasma emission observation, high-energy detectors and direct measurements by radiation interaction. Many systems focus on measurements of the core plasma, but the need for a holistic view of the open-field-line plasma continues to push more focus off the mid-plane of the machine and into other regions of the device: the full CV, inner and outer divertors, and formation sections. The diagnostics fulfill two roles: detailed measurements of machine dynamics for post analysis and more general measurements, which can be processed in real time for plasma control. A wide range of plasma parameters and machine conditions are followed during the evolution from seed FRC to a much hotter and higher energy state by the diagnostic suite. The signals are distributed to four screened rooms located near the machine and a diagnostic lab which houses sensitive optical equipment. The thousands of signal channels produce a significant amount of data for every C-2W shot, typically on the order of 10 GB in total, including analysis movies and computations. The raw data are post-processed into plasma parameters and then stored in a physics database for further data analysis. Some raw data, like magnetic probe signals and biasing electrode currents and voltages, are processed at lower fidelity during a plasma shot through the RTPCS used in active feedback control of the plasma [16, 17].

3. C-2W experimental results

3.1. Enhanced performance in advanced beam-driven FRCs

Producing a stable FRC for effective NBI is one of the most important elements in obtaining a beam-driven FRC plasma state because the injected fast ions typically take ~ 1 ms to accumulate and develop sufficient pressure inside the FRC. This plasma state was initially obtained in C-2U via the synergistic effects of edge biasing and NBI, where FRC plasma was maintained for 5+ ms [11]. In C-2W with significantly upgraded key subsystems from C-2U, as previously reported in [4], FRC performance and its superior plasma state have been considerably advanced and sustained in steady state up to 30 ms (limited by the NB pulse length). Furthermore, C-2W NB systems have recently been upgraded to extend its pulse length to 40 ms, at which some dedicated NB system optimizations have also been conducted to further enhance FRC plasma performance; details are described in section 3.3 below.

In recent C-2W experiments, controlled external magnetic field profiles throughout the machine and proper gas injection have led to more effective edge biasing from electrodes to globally stabilize FRC plasma. This allows improvements in

the efficiency of NB-to-FRC coupling as well as the accumulation of more fast ions inside the FRC; therefore, more plasma heating and current drive via NBI are obtained. Due to the synergistic effect of efficient edge biasing and NBI as well as by dedicated plasma and machine optimization efforts in C-2W, the FRC plasma state has significantly advanced to a much higher level than the previously reported good FRC condition (e.g. shot #114534, also seen in figure 9 of [4]) as shown in figure 2. Note that for simplicity and performance comparison at a quiescent phase in two different shots, initial FRC formation phase ($t < 5$ ms) is not shown in the figure. Some highlights and key features of the recent enhanced plasma performance (for instance in shot #143348) are as follows: (a) the excluded-flux radius of the FRC is maintained at ~ 0.45 – 0.5 m until NB termination at $t \sim 40$ ms, while FRC length and volume can be increased and controlled by external magnetic field reshaping during a shot in either feedforward or feedback control mode as designed [16, 17]; (b) the estimated trapped poloidal flux ϕ_p (based on the rigid-rotor model [1]) is significantly increased up to ~ 16 mWb at an equilibrium phase, indicating the effect of NB current drive; (c) the plasma density (i.e. internal plasma pressure) goes up by 50%–100% during a shot depending on magnetic field shaping and particle fueling scheme, which is also indicative of injected fast-ions accumulation; (d) as a result of the internal pressure increase, the plasma energy also goes up significantly; and (e) based on an equilibrium reconstruction, fast-ion pressure is comparable to or greater than thermal plasma pressure at a quiescent phase. In this particular shot #143348, the external magnetic field profile in the confinement section was reshaped during $t = 4$ – 24 ms using Google's Optometrist Algorithm [28], after which it stayed constant until the end of the discharge; some details of the magnetic field reshaping are described in the following section 3.2. Furthermore, under some operating conditions, the electron temperature T_e of FRC plasmas at a quiescent phase has successfully reached up to ~ 1 keV at the peak, for the first time, and >0.75 keV averaged inside the FRC separatrix, measured by a mid-plane Thomson scattering system [29]; an example of such a high-temperature FRC plasma state is shown in figure 3.

FRC performance is well correlated with both NBI and edge biasing from electrodes. Figure 4(a) shows plasma total energy E_{tot} (at the peak value of each shot) as a function of the NB total injected power (estimated by the actual NB current) and edge-biasing electrode voltage for ensembled C-2W shots in the recent experimental campaign. As can be clearly seen, higher E_{tot} is obtained with higher NBI power and biasing voltage on electrodes, which indicates the importance of these systems in producing high-energy FRC plasma conditions. E_{tot} is estimated by integration of one-dimensional (1D) pressure reconstruction along the geometrical axis (z -axis), where the 1D reconstruction corresponds to a paraxial approximation (highly elongated plasma) with the assumption of a sharp boundary between the plasma and the surrounding magnetic field. A similar statistical analysis for FRC thermal energy (E_{th} ; defined as $3/2 \cdot \int p dV_s$, where p and V_s are FRC plasma pressure and volume, respectively [1]) was also performed,

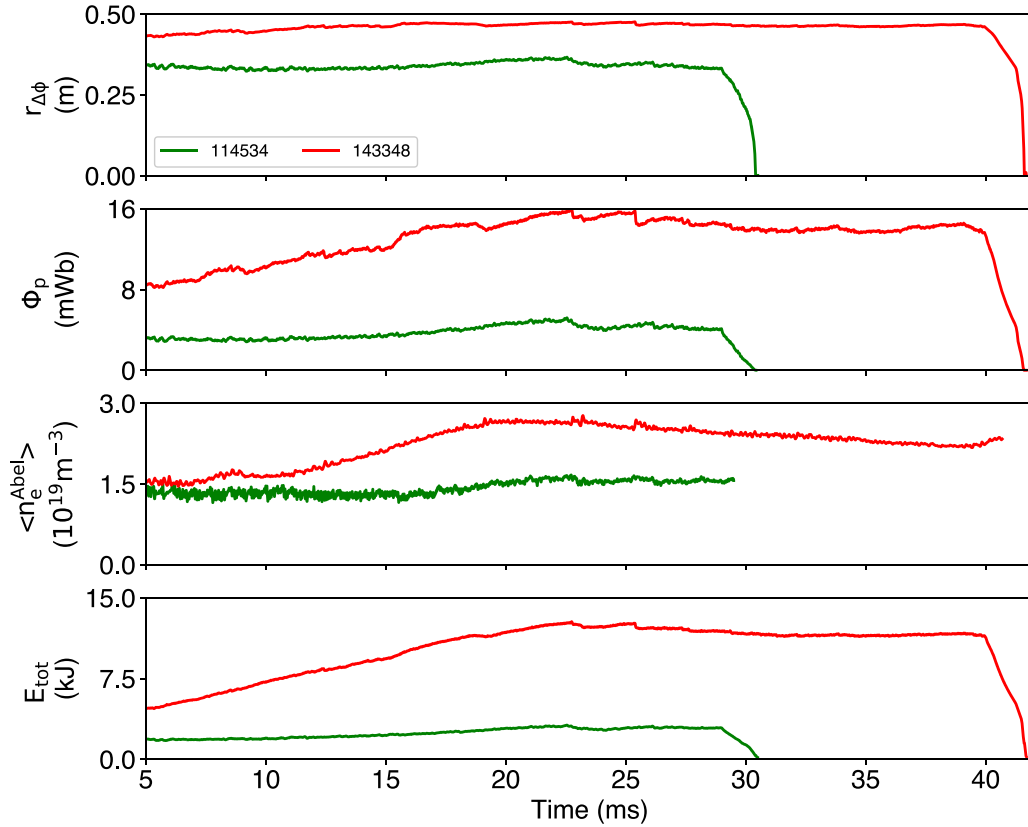


Figure 2. Time evolutions of excluded-flux radius ($r_{\Delta\phi}$), trapped poloidal magnetic flux (ϕ_p), Abel-inverted averaged electron density inside the FRC separatrix (n_e), and total plasma energy (E_{tot}) for recent C-2W shot #143348 (red), compared with previously reported good shot #114534 (green) [4]. Note that all eight NBs are terminated at $t \sim 29$ ms in shot #114534 and $t \sim 40$ ms in shot #143348 and that Abel-inverted electron density traces are truncated near the end of plasma discharges (shortly after NB termination) due to axisymmetry breaking by plasma instabilities.

which indicates a very similar trend and characteristics as seen in figure 4(a). The value of E_{tot} appears to be approximately 1.5 times higher than that of E_{th} based on experimental results, indicating that there is a large amount of plasma and energy in the open-field-line/SOL region. Figure 4(b) shows a comparison of E_{tot} as a function of NBI total power between recent C-2W shots (red circles) and the previously reported ensemble of shots (blue triangles; data from figure 21 of [4]); note that biasing-electrode operating conditions in both cases were similar to each other for a fair comparison. The figure clearly shows that E_{tot} in the recent campaign is at much higher level (>50% higher) overall compared to the old C-2W campaign, achieving $E_{\text{tot}} \sim 13$ kJ with high NBI power.

To further ascertain the contribution of fast ions in the steady-state plasma, TAE has developed an equilibrium reconstruction code, SEQUOIA [30], using the direct experimental inputs such as experimental density and temperature profiles, magnetic data from magnetic probes and flux loops at the vessel wall and NB input data. Using the experimental profiles, the plasma equilibrium is constructed by solving Ampere's law including the diamagnetic thermal plasma current and the kinetic fast-ion current. The thermal plasma current is calculated from the experimental profiles of density and temperature measured at the mid-plane. The fast-ion

current is calculated by modeling the NB source term with a Monte Carlo code, with beam trapping due to ionization and charge exchange, and evolving the fully kinetic ion orbits. The fast ions are subject to Coulomb collisions with the background plasma, charge-exchange losses against the background neutral density and pitch-angle scattering against non-axisymmetric magnetic perturbations. These transport effects create a slowing-down distribution, and they scatter some of the betatron orbits into figure 8, type 1, and drift orbits, leading to a change in radial fast-ion current profile. The strengths of the three sink term models are varied to minimize the difference between the measured magnetic flux data and simulated data, i.e. until the sink terms balance the source term, and a steady-state equilibrium is achieved. In this iterative simulation procedure, the plasma goes from low-beta mirror to high-beta mirror and finally to the field-reversed state (i.e. FRC state). For our recent C-2W shot (e.g. #143348) in the equilibrium state, the reconstructed plasma state is an FRC; the radial pressure profile of the cumulative thermal plasma pressure, magnetic pressure and fast-ion pressure is shown in figure 5. It clearly shows the significant fast-ion contribution in the core of the FRC, where the fast-ion pressure appears to be about 1.5 times higher than the thermal plasma pressure in the recent high-performing C-2W shots.

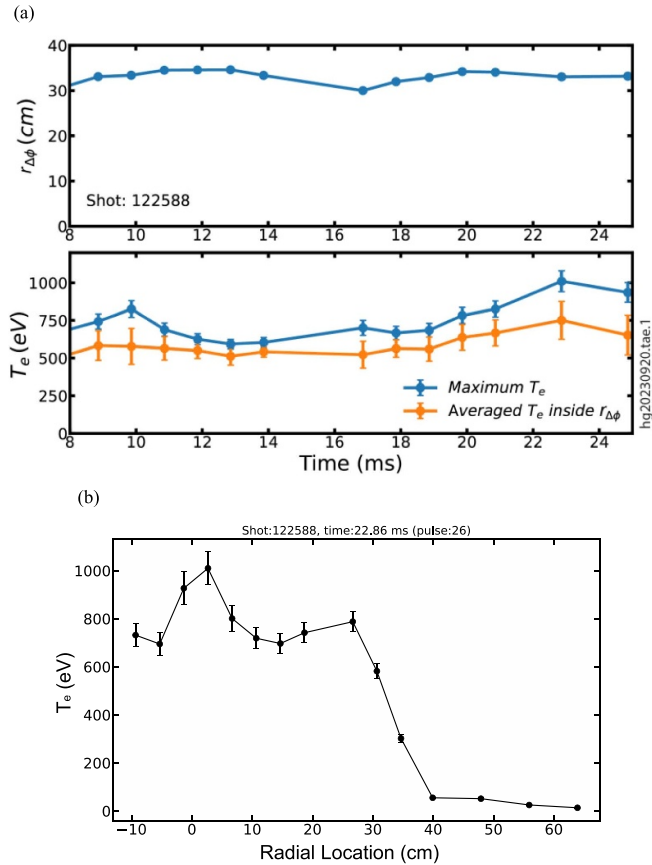


Figure 3. (a) Time evolutions of excluded-flux radius, maximum and averaged electron temperatures inside the FRC separatrix in shot #122588, measured by a mid-plane Thomson scattering system. (b) Radial profile of the electron temperature for the same shot at $t \sim 23$ ms, achieving a peak T_e up to ~ 1 keV in the FRC core region; note that the center of the radial location represents the machine axis.

At TAE, besides some specific and physics-focused experiments in C-2W, a dedicated system and plasma optimization campaign has been routinely conducted from time to time with hardware/configuration changes and upgrades, e.g. optimizations focused on magnets, NBI, biasing electrodes and gas injection systems independently, or optimizing various systems together. In the following sub-sections, three independent optimization campaigns and processes focused on the magnetic field profile, the NB system and the edge-biasing system are described.

3.2. Optimizations of magnetic field profile

Both formation and sustainment/ramp-up of the FRC system are critically dependent on the profile of the externally applied magnetic field. This includes the shape of the CV magnetic field, mirror ratios, formation section background field and field flaring/expansion in the divertors. As the dynamics of the system changes during a shot, the magnetic field must also be reshaped to properly provide the magnetic confinement required. This dynamical process starts before any plasma is generated and continues after the shot comes to an end. There

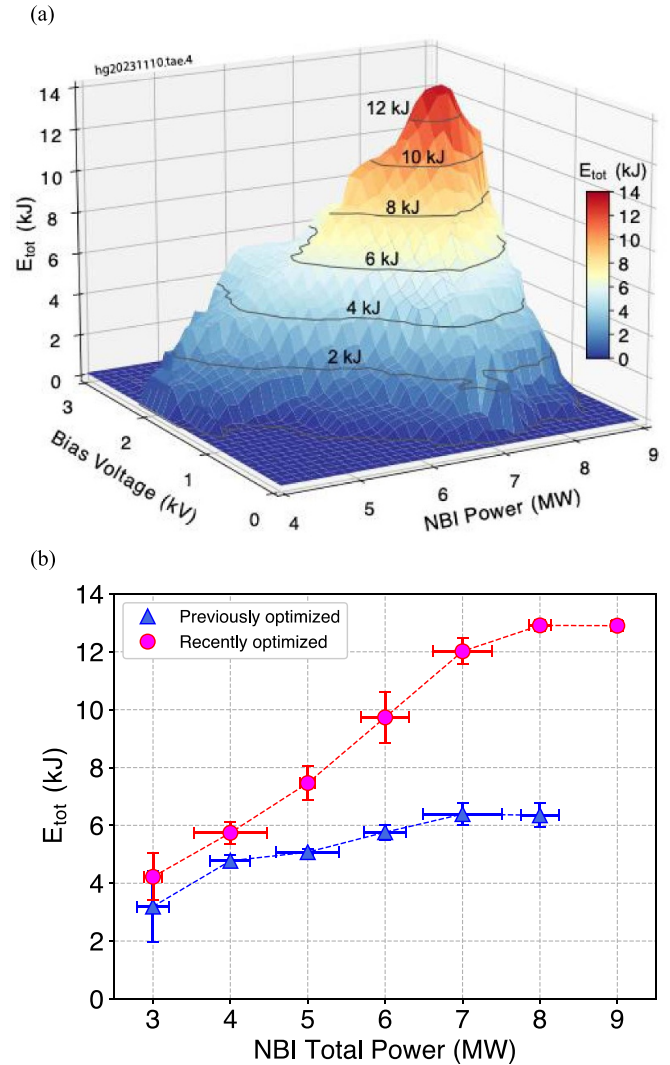


Figure 4. (a) Total plasma energy E_{tot} (at peak value) as a function of NBI power (total injected neutral power from 8 NB injector systems) and edge-biasing electrode voltage for recent ensembled C-2W shots at a quiescent phase. (b) Comparison of E_{tot} as a function of NBI power between recent shots (red circles) and the previously reported ensembled data (blue triangles; data from figure 21 of [4]), where bias-electrode operating conditions were similar in both cases for a fair comparison.

are several stages in the process: initial field configuration, target establishment configuration and steady-state configuration (rarely a static case in terms of external magnetic field). Since the initial field configuration stage was previously reported in [7], this paper only focuses on the target establishment and steady-state configuration stages, particularly in the confinement section.

Once the FRC plasma is well established in the CV and the NB current drive is sustaining the diamagnetic current, the plasma pressure inside the FRC can increase. To contain the increase in pressure while keeping the FRC size nearly constant, the magnetic field structure can be modified in a couple of ways. First, the magnitude of the magnetic field is increased at the mid-plane; on its own this will only arrest the expansion of the FRC in the radial direction. Second, the length of

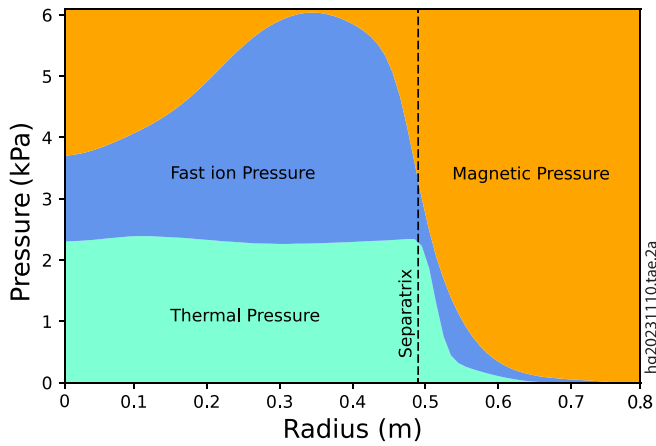


Figure 5. Radial profiles of cumulative magnetic pressure (orange), fast-ion pressure (blue) and thermal plasma pressure (green), obtained by the equilibrium reconstruction code, SEQUOIA [30]. This clearly shows the dominance of the fast-ion pressure inside the FRC separatrix in recent C-2W shot #143348 at a quiescent phase.

the FRC plasma can be increased; to accomplish this, magnet currents near the end of the CV are decreased. Figure 6(a) shows sample waveforms of the equilibrium magnet/coil current (EQ1–4) in the confinement section, where a pair of EQ1 magnets is located near the machine mid-plane and the other pairs are spread out axially as illustrated in figure 1. In this particular shot, magnet/coil currents during $t = 3–20$ ms are adjusted to produce external magnetic field profiles such as the ‘U-shaped’ profile early in time for target FRC establishment and then modified to a ‘W-shaped’ profile later in time for steady-state operations, as depicted in figure 6(b). By performing such a dynamic coil-current adjustment and magnetic field reshaping, the generated and confined FRC plasma becomes highly elongated axially in the CV. Note that this type of dynamic coil-current waveform was obtained through a dedicated experimental campaign with Google’s Optometrist Algorithm [28] to achieve high stored energy (e.g. thermal energy E_{th} and total energy E_{tot}) of the FRC plasma as well as to enhance plasma performance in general. As an example of this magnetic field reshaping (from a U-shaped to a W-shaped field profile) and plasma length control, figure 7 shows the time evolution of E_{tot} as a function of FRC length during the magnetic-field reshaping. The data are from typical plasma discharges (under similar operating conditions but five non-repeated shots), and their parameters are at $t = 5, 15$ ms and when maximum E_{tot} is obtained in each shot (typically $t > 20$ ms). It is clearly shown that the total plasma energy is effectively increased as the FRC plasma gets elongated axially via magnetic-field reshaping.

As the FRC plasma gets longer it typically becomes axially unstable. However, with the use of the RTPCS, the plasma can be affected to remain centered in the confinement section (or move to any desired axial location) [4, 16, 17]. By reading and interpreting plasma diagnostics during a shot, the feedback system can affect the length, shape, location, density and overall stability of the plasma by changing various

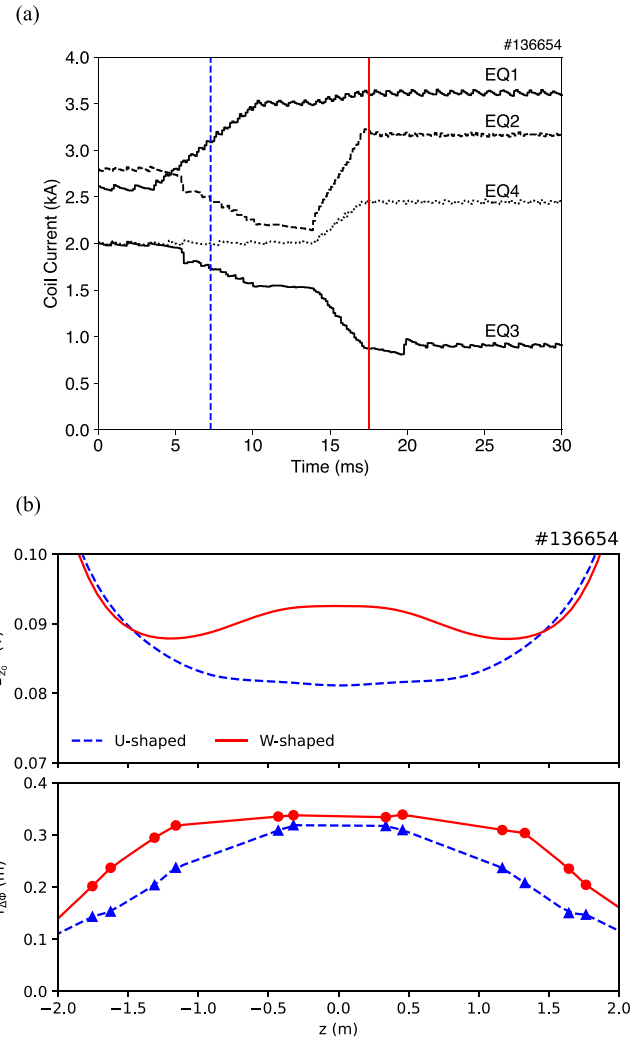


Figure 6. (a) Equilibrium magnets (EQ1–4) coil-current time evolution, only showing the $t = 0–30$ ms time window for simplicity. (b) External axial magnetic field and excluded-flux radius axial profile at $t \sim 7.5$ ms (blue dashed lines) and $t \sim 17.5$ ms (red solid lines), where reshaping of the axial magnetic field profile from U-shaped to W-shaped as well as elongated FRC length can be clearly seen.

magnet currents, controlling edge-biasing electrode voltage and current, varying energies of the tunable NBs and modifying gas fueling rates. By specifying a desired plasma condition before the shot, the RTPCS will read several data streams during the shot and adjust actuators to achieve the desired plasma condition [17].

3.3. Optimizations of neutral beam systems

Reliable operation of the NBI systems is critical to plasma performance on C-2W. The eight NBI systems generally operate at the designed specification, but small modifications to beam parameters can lead to greater plasma performance. Three of these beam-related parameters are the injected beam current, I_{inj} , the beam energy, E_{NB} and beam impact parameter, b .

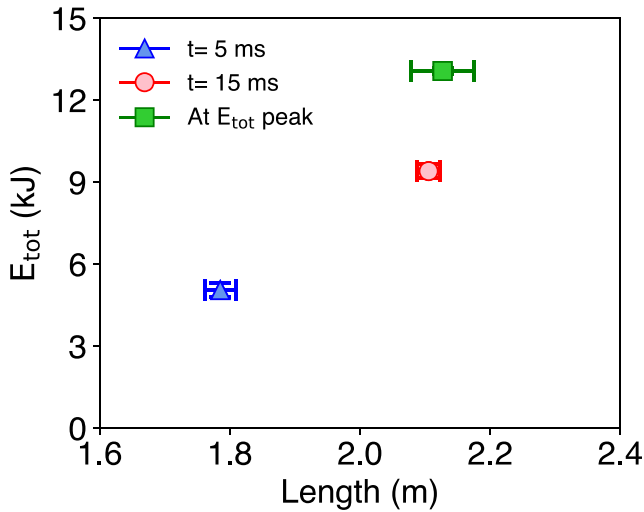


Figure 7. Time evolution of total plasma energy as a function of FRC length during magnetic field reshaping (from U-shaped to W-shaped field profile). Data is from typical plasma discharges (similar operating conditions but five non-repeated shots) whose time stamps are at $t = 5$, 15 ms and when maximum E_{tot} is obtained in each shot (typically $t > 20$ ms).

A strong correlation has been found between I_{inj} and E_{tot} . In this context, I_{inj} is defined as the NB current minus losses from the vacuum duct and reionization. Following the relationship between the NB current and the beam size described by the Child–Langmuir law [31], each NBI system generally operates at a specific current to minimize beam size, limiting losses to the vacuum duct. This is called the nominal beam current, I_{nominal} , and is monitored shot-to-shot by multiple diagnostics. The time-integrated injected beam power and horizontal position are measured at the entrance port of each NB via a wire calorimeter [32]. The vertical position and beam shine-through are inferred measurements made by an array of secondary electron emission detectors located in the NB dump [33]. The NBI systems are optimized by manipulating the beam neutralization gas pressure, beam position and ion source perveance. The optimization of I_{inj} is thoroughly outlined in [22].

As mentioned above, I_{inj} is directly correlated to increased plasma performance on C-2W. Specifically, as I_{inj} increases, total plasma energy E_{tot} increases, independent of beam energy, as shown in figure 8(a). For the three tunable beam energy cases (E_{tunable} at 15 keV, 25 keV and 30 keV), the data points and error bars are the average and standard deviation of the upper 20% of E_{tot} values during a plasma optimization campaign, and I_{inj} is normalized by the value of I_{nominal} at 15 keV. Furthermore, an increase in I_{inj} can be attained by increasing the injected NB currents past their nominal values, as suggested by experiments on the Joint European Torus (JET) [34]. For a small increase in ion current, up to 10% of the total current, I_{inj} increases despite the increased loss to

the vacuum duct due to the beam size increase. It is seen in figure 8(a) that in the regime where $I_{\text{inj}} > I_{\text{nominal}}$, a non-linear increase in E_{tot} occurs. The gains in NB current are finite; however, as losses accumulate in the vacuum duct, a plasma can form causing a beam stoppage.

There are a couple of mechanisms that can lead to the non-linear increase in plasma performance. The increased fueling from NBI could increase the plasma density inside the core region, which would lead to better beam capture. Also, the increases in NB current would lead to an increase in fast-ion current, and thus, an increase in fast-ion pressure. Note that beam shine-through for the data set in figure 8(a) is $15 \pm 5\%$ independent of I_{inj} value, so it is not the case that beam capture is increasing. What does occur, however, is that the applied magnetic fields from the equilibrium coil set are able to be increased without affecting plasma stability. This suggests that the increase in NB current is leading to an increase in fast-ion pressure, which can then be balanced by external pressure from the magnetic field. The change in applied magnetic field, measured at the CV wall as external magnetic field, B_{ext} , can be seen in figure 8(b).

In addition to the NB current, the beam energy plays a role in fast-ion pressure as well. The dependence of B_{ext} on E_{tunable} and I_{inj} during this particular plasma optimization campaign is also shown in figure 8(b), where the data points and error bars are the average and standard deviation of the upper 20% of E_{tot} values during the campaign. As mentioned above, for $E_{\text{tunable}} = 15$ keV case, there is a non-linear effect above the nominal current, as shown in figure 8(a). As the energy of the tunable NBs is increased to $E_{\text{tunable}} \sim 25$ keV, B_{ext} increases with I_{inj} as well. The optimal magnetic field is higher for both $E_{\text{tunable}} \sim 25$ keV and ~ 30 keV ensembles when compared with the $E_{\text{tunable}} = 15$ keV data for the same I_{inj} . This suggests that the fast-ion pressure is increasing with both I_{inj} and E_{tunable} , enabling higher compression by the external magnetic fields, and thus, larger plasma energies. There are two operational notes worth mentioning here. First, the tunable energy beams provide less beam current as the beam energy increases due to conditioning and power supply limitations. Second, the data in figures 8(a) and (b) are from an experimental campaign limited in scope, and the data set presented here is only meant to demonstrate the relationships, where the three beam energy cases (15 keV, 25 keV and 30 keV) included 550 shots, 45 shots and 47 shots, respectively, and the large shot number discrepancy between the 15 keV case and the higher energy cases is mainly due to the required time for their dedicated beam conditioning.

The beams are normally aimed at $b \sim 0.2$ m radially, which can be changed without a vent up to a couple of degrees; this translates to a ± 3 cm variation from the nominal b . As part of an additional NBI study and optimization, a set of scans of different magnetic field configurations and effective beam impact parameters b_{eff} , defined as the current-weighted average beam impact parameter, was conducted. Figure 9 shows, as one particular example, the dependence of the trapped

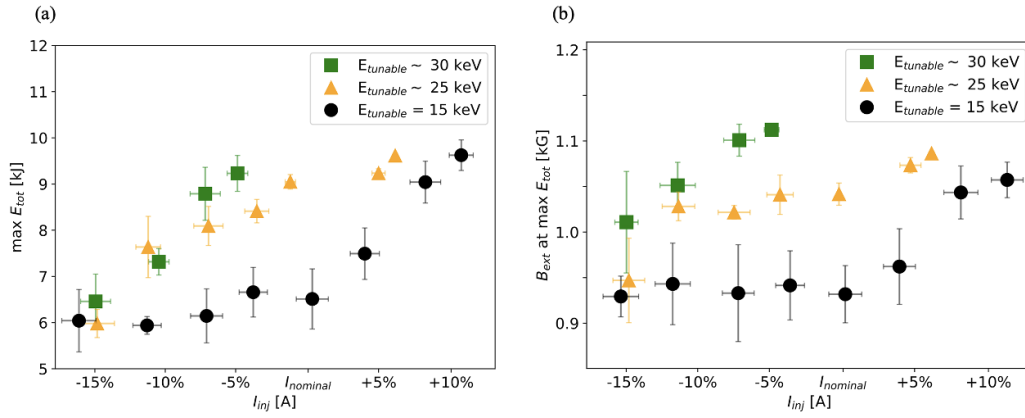


Figure 8. (a) Dependence of plasma stored energy E_{tot} on injected neutral beam current I_{inj} normalized by the nominal beam current $I_{nominal}$ at 15 keV for three $E_{tunable}$ cases (15 keV, 25 keV and 30 keV), where the data points represent the average of the top 20% highest performing shots, and the error bars reflect the standard deviation (using 550 shots, 45 shots and 47 shots in 15 keV, 25 keV and 30 keV cases, respectively). (b) Dependence of external magnetic field (B_{ext}) measured at the CV wall at the point of maximum total stored energy with respect to I_{inj} normalized by $I_{nominal}$ for the three $E_{tunable}$ cases.

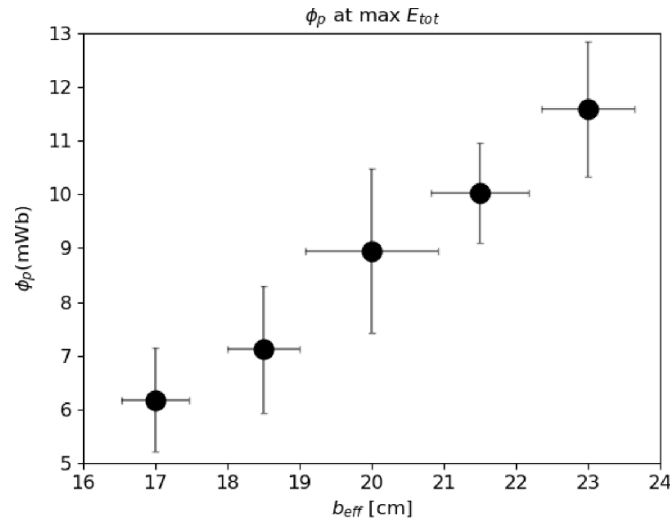


Figure 9. Trapped poloidal flux ϕ_p (estimated from the rigid-rotor model) as a function of effective beam impact parameter b_{eff} for ensemble shots in W-shaped magnetic field configuration with B_{ext} in the range of 0.78–0.93 kG.

poloidal flux ϕ_p (based on the rigid-rotor model) on the effective beam impact parameter b_{eff} under similar W-shaped magnetic field configurations with B_{ext} in the range of 0.78–0.93 kG. It is found that increasing the beam impact parameter yields an increase in ϕ_p , but it appears to be independent of B_{ext} amplitude. The same trend and characteristics were observed in the U-shaped magnetic field configuration case as well. The increase in ϕ_p from b_{eff} suggests an increase in NB current drive. Overall, the main effect of the larger impact parameter is an increase in the plasma size during this limited scan.

Lastly, there are other beam-related changes to the C-2W machine that have recently occurred in addition to the modifications and optimizations mentioned above; namely, the angle of NBI relative to the geometrical axis (z -axis). The four tunable-energy NB angles were changed from 70° to 57° ,

basically injecting beams at a shallower angle in the z direction to increase the parallel component of the beam energy and the axial distribution of the fast-ion population. It has been theorized that greater axial beam pressure and distribution would lead to a longer FRC. Initial experiments after the modification confirmed this assertion [25]. Since this experimental campaign with different NBI angles is still underway, more detailed experimental results and observations will be reported elsewhere in the future.

3.4. Optimizations of edge biasing for plasma rotation control

Optimizing edge biasing is also crucial for enhanced performance in the C-2W device. Edge biasing serves as a key mechanism within our FRC devices, tasked primarily with inducing $E \times B$ rotation in the SOL plasma opposite to the NBI direction

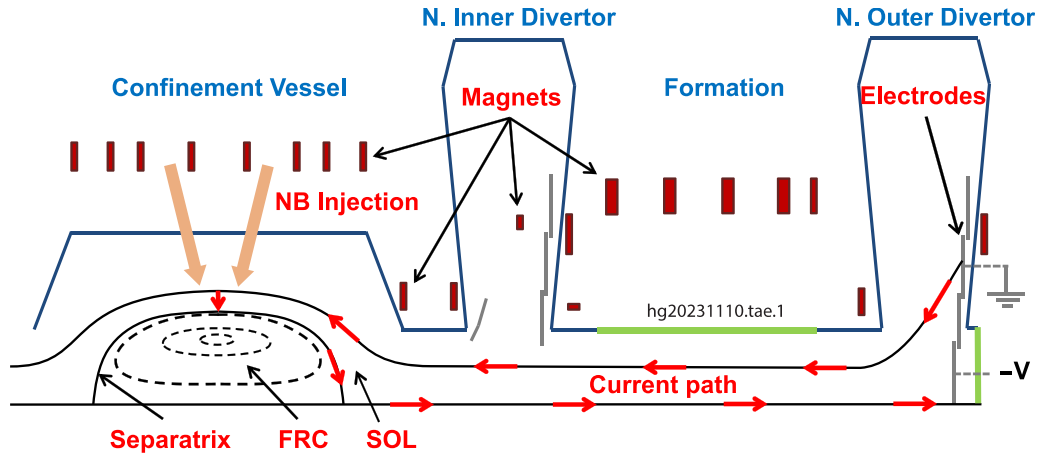


Figure 10. Simple schematic of electrode biasing in C-2W (showing only north half of the device for simplicity). Applied potentials at end electrodes are translated along \vec{B} -field lines to create $\vec{E}(r)$ in the SOL at the FRC plasma edge. Red arrows represent one particular and ideal path of useful currents for a negative biasing scheme, while a path of lost currents in the open-field-line region (in other words, not reaching the central region) is not shown for simplicity (see figure 4 of [4] for another simplified sketch of biasing current propagation from electrodes, including a path of lost currents).

(ion-diamagnetic direction; the same direction as natural FRC rotation) [9, 12]. This rotation mitigates MHD instabilities and reduces cross-field energy and particle transport from the FRC core [4, 13]. A significant sheared flow of SOL plasma, encompassing both electrons and thermal ions, is necessary to balance the azimuthal momentum imparted by NBs. With improvements in NB performance in terms of beam energy and current, and as magnetic fields are elevated along with pressure gradients in the SOL, an increase in effective bias currents becomes imperative. These currents are essential to manage the natural spin-up of the core plasma and maintain stability.

For optimal control over plasma rotation, a robust electrical connection and current flow from the end electrodes to the SOL and the FRC region through open-field lines, where a negative bias voltage is applied to the innermost electrode in the outer divertor. Note that red arrows represent one particular and ideal path of useful currents for a negative biasing scheme, while a path of lost currents in the open-field-line region (i.e. not reaching the central region) is not depicted for simplicity. Applied potentials display axial and radial variations from the boundary toward the center of the CV due to field expansion and density gradients. Enhancing mirror fields in the confinement section and magnetic-mirror plugs, along with precise gas injection targeting to the biased field lines, is crucial for augmenting ion mobility toward the axis and boosting the effective bias current from the divertor region into the CV.

In C-2W, dedicated Doppler spectroscopy diagnostics (both active and passive) are employed to ascertain local impurity profiles and deduce radial electric field (E_r) profiles in the CV from radial momentum balance, as detailed in

referenced studies [35–37]. Through meticulous lineshape analyses of the emitted spectra, vital ion parameters such as temperature, velocity and density can be discerned from the width, shift and area (intensity) of the emission lines, respectively. In particular, the azimuthal rotation velocity of high charge-state impurities (e.g. O^{4+}) is sensitive to the $E_r \times B_z$ azimuthal drift component and is routinely monitored and used as a quantitative proxy to assess the efficacy of the electrode-biasing system's contribution to overall plasma rotation [37].

To illustrate the effect of edge biasing on plasma performance, figure 11(a) depicts a time sequence of several signals from a plasma shot with electrode biasing terminated at $t \sim 28$ ms. Initially, the FRC plasma is sustained in quasi-steady state with a negative biasing voltage (-1.7 kV) applied on the innermost electrodes inside both outer divertors. When this biasing scheme is implemented, O^{4+} impurities are subjected to the potential drop across the SOL and rotate swiftly in the electron-diamagnetic direction ($+\theta$ direction). At $t \sim 28$ ms, the applied potential is deliberately lowered to nearly zero within approximately 0.25 ms. Removal of the biasing reverses the rotation of O^{4+} impurities to the ion-diamagnetic direction ($-\theta$ direction), aligning with the drift direction of fast ions from NBs. Subsequent to the bias removal, an increase in MHD mode amplitude is observed from magnetic probe signals [38, 39], specifically toroidal mode number $n = 1$ (wobble) and 2 (rotational) modes. Although the plasma continues to be maintained during the ensuing bias-free time interval ($t > 28$ ms), the bias termination adversely affects plasma pressure and confined thermal energy, as evidenced by the gradual decrease in the plasma radius. Generally, in this condition, the plasma continues to spin up and the growth of detrimental instabilities typically leads to a loss of FRC stability and sudden collapse of the

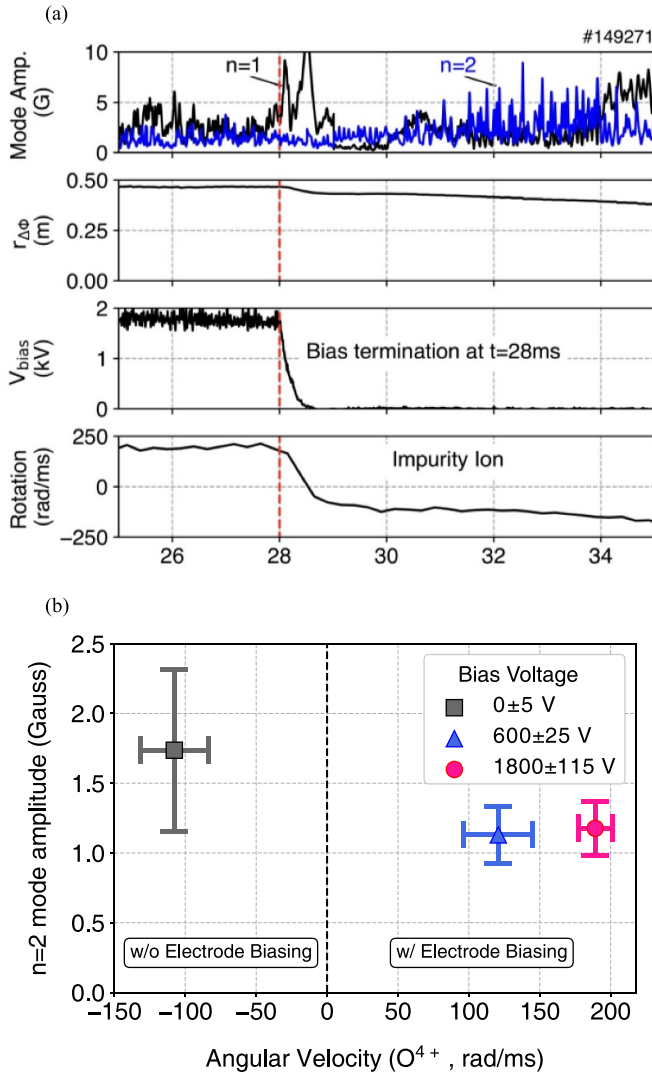


Figure 11. (a) Time evolutions of $n = 1$ and 2 mode amplitudes, excluded-flux radius, bias voltage and core-averaged azimuthal angular velocity of O^{4+} impurities, where edge biasing is terminated at $t \sim 28$ ms (red dashed lines). (b) Impurity ion angular velocity versus $n = 2$ mode amplitude for different (negatively applied) biasing voltage operations.

FRC plasma. Figure 11(b) further illustrates the correlation between the core-averaged impurity rotation under different biasing voltage conditions and the average amplitude of the $n = 2$ mode.

Throughout an optimization campaign for the machine, the core-averaged impurity rotation was measured under various bias input power conditions (bias voltages approximating 1–3 kV and bias currents around 1–2.5 kA). Figure 12 shows the total plasma energy as a function of O^{4+} angular velocity under various electrode-biasing input powers. The figure indicates a proportional increase of the total plasma energy with increasing bias input power, which is consistent with figure 4(a). However, it is important to recognize that while higher bias voltages and currents generally enhance plasma performance in C-2W, they also necessitate a nuanced balance

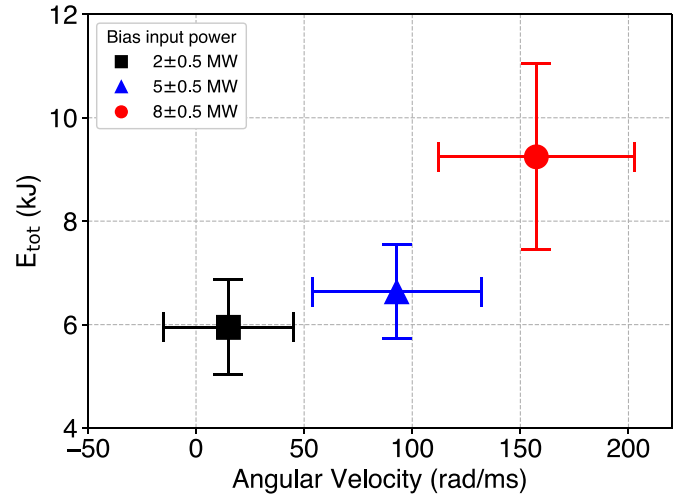


Figure 12. Total plasma energy as a function of impurity ion (O^{4+}) angular velocity under various electrode-biasing input powers. All positive rotation velocities shown here correspond to scenarios when a negative biasing scheme is utilized. Higher performance shots are generally achieved with increasing bias input power.

due to the interplay of multiple machine and plasma variables. Overstepping in these conditions can lead to complications such as arcing, neutral recirculation and plasma detachment on the electrodes.

To mitigate such risks, C-2W employs several strategies, including titanium gettering on electrode surfaces to avert neutral build-up, the RTPCS [17] for bias-current management to prevent excessive current and electrode damage due to arcing and an optimized electrode geometry and biasing scheme. The RTPCS enables the electrode-biasing system to operate in ‘current control’ mode, as illustrated in figure 13. This mode of operation differs from the standard ‘voltage control’ mode, when predefined and unchanged voltage waveforms are applied during the course of the discharge and can inadvertently lead to uncontrolled current surges attributable to evolving plasma conditions. To prevent detrimental current spikes due to dynamic and uncontrolled changes in plasma conditions near the electrode plates, the RTPCS allows the setting of a target current threshold, enabling real-time modulation of the electrode power supply voltage to maintain the bias current within prescribed safety margins. As an example, figures 13(a)–(c) show the time evolution of one particular shot which had arcing events on electrodes at around $t \sim 8$, 21 and 22 ms. The target current threshold for this shot was set to 4 kA. Once the bias current reached the threshold, the bias voltage quickly dropped and controlled the spike current in real time. After the arcing (i.e. over bias current) was mitigated, the bias electrodes re-energized the FRC by increasing the voltage slowly. Figure 13(d) shows an image of the bias electrodes during one of the arcing events at around $t \sim 21$ ms using a fast-framing camera mounted on the divertor [40]. Bipolar arcing occurred between electrode plates, resulting in a shorted circuit and the bias current rapidly increased. The capability for real-time control of the bias

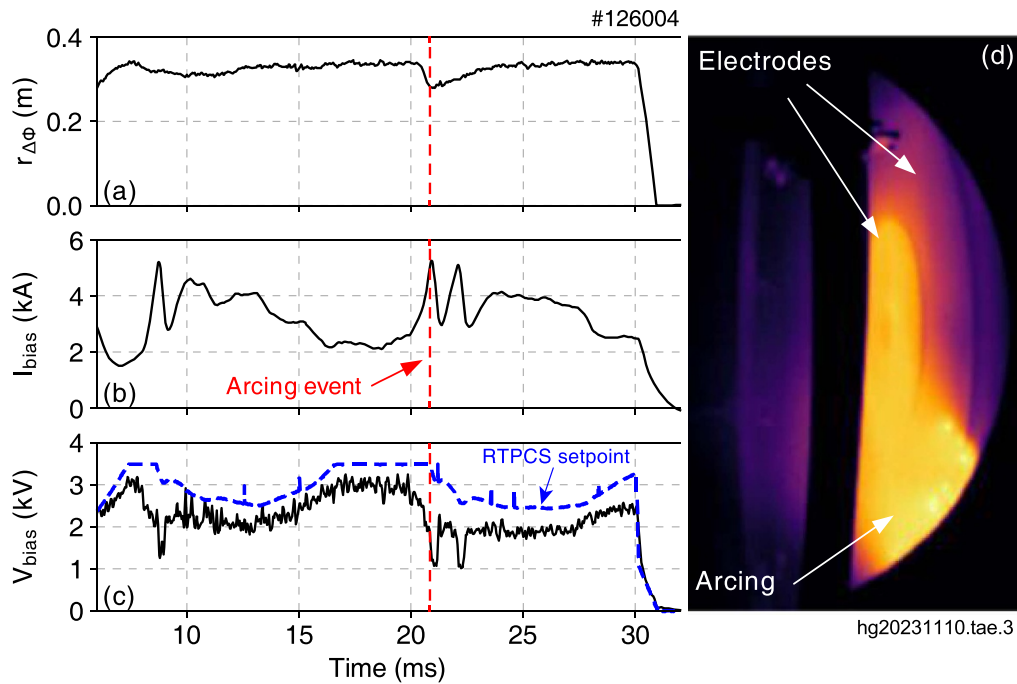


Figure 13. Time evolutions of (a) excluded-flux radius, (b) bias current and (c) bias voltage. (d) Image from side-on fast-framing camera mounted on the outer divertor, where concentric electrodes with bright spots on the bottom of the image can be seen at the time of arcing event. The vertical red dashed lines (at $t \sim 21$ ms) indicate the time of the picture image for one particular arcing event, and the blue dashed line represents the bias voltage setpoint of the RTPCS adjusted in real time. In this particular shot, the bias electrode system is terminated at 30 ms.

current, integrated with data from auxiliary diagnostics monitoring the plasma state, has been instrumental in facilitating performance enhancements of the C-2W device while mitigating the risks of equipment damage for reliable and consistent machine operations.

4. Summary

The C-2W NB system was recently upgraded to extend its pulse length from 30 ms to 40 ms, which allowed for longer steady-state operations as well as enhanced FRC plasma performance. In addition, Google's advanced Optometrist Algorithm and in-house active plasma control systems were used in C-2W to further enhance plasma performance and machine operation reliability. Dedicated plasma and machine optimization campaigns, particularly focused on the external magnetic field profile, NBI and edge-biasing optimizations, led to a superior FRC plasma performance; for instance, achieving a total plasma energy of ~ 13 kJ, a trapped poloidal magnetic flux of ~ 16 mWb, and plasma sustainment in steady state up to 40 ms which is limited by the NB pulse duration. Furthermore, under some operating conditions, the electron temperature of FRC plasmas at a quiescent phase successfully reached up to ~ 1 keV at the peak inside the separatrix for the first time. The plasma performance was well correlated with the injected beam current and power as well as with FRC length. C-2W operations have now reached a mature level where the machine can produce hot, stable, long-lived, repeatable plasmas in a well-controlled manner.

Acknowledgments

The authors wish to thank the entire TAE Fusion and Power Solutions Teams for their dedicated work and contributions to the C-2W program, as well as to thank external collaborators including Google and our shareholders who made this exciting fusion research possible at TAE.

ORCID iDs

H. Gota <https://orcid.org/0000-0001-6475-2912>
M.W. Binderbauer <https://orcid.org/0000-0002-2698-4744>
J.B. Titus <https://orcid.org/0000-0002-6457-3751>
M. Nations <https://orcid.org/0000-0002-7795-1555>
T. Roche <https://orcid.org/0000-0003-0840-4731>
E. Trask <https://orcid.org/0000-0003-4984-6579>
T. DeHaas <https://orcid.org/0000-0003-3822-2074>
S.A. Dettrick <https://orcid.org/0000-0002-1756-4625>
E.M. Granstedt <https://orcid.org/0000-0002-7691-4883>
D.K. Gupta <https://orcid.org/0000-0003-4849-1198>
S. Gupta <https://orcid.org/0000-0001-5688-4122>
S. Korepanov <https://orcid.org/0000-0002-6118-729X>
R.M. Magee <https://orcid.org/0000-0001-6697-7891>
T. Matsumoto <https://orcid.org/0000-0002-3217-3622>
J.A. Romero <https://orcid.org/0000-0001-7585-1350>
K. Zhai <https://orcid.org/0000-0002-8432-3696>
L. Schmitz <https://orcid.org/0000-0003-1346-0914>
Z. Lin <https://orcid.org/0000-0003-2007-8983>

S. Krasheninnikov  <https://orcid.org/0000-0002-0786-5440>
 E.A. Baltz  <https://orcid.org/0000-0002-4827-1542>
 J.C. Platt  <https://orcid.org/0000-0002-5652-5303>
 E.V. Belova  <https://orcid.org/0000-0002-1525-1027>
 T. Asai  <https://orcid.org/0000-0001-9440-0117>
 A.I. Smolyakov  <https://orcid.org/0000-0002-4975-2743>
 I. Allfrey  <https://orcid.org/0000-0001-8031-5384>
 J. Barrett  <https://orcid.org/0009-0003-7298-7182>
 M. Beall  <https://orcid.org/0000-0002-5070-6824>
 N.G. Bolte  <https://orcid.org/0000-0002-3702-4650>
 A. Bondarenko  <https://orcid.org/0000-0003-0599-4721>
 F. Ceccherini  <https://orcid.org/0000-0003-3377-6932>
 R. Clary  <https://orcid.org/0000-0001-8500-4139>
 C. Deng  <https://orcid.org/0000-0003-1092-9959>
 A. Fareed  <https://orcid.org/0000-0002-9278-8143>
 L. Galeotti  <https://orcid.org/0000-0003-3426-2087>
 S. Galkin  <https://orcid.org/0000-0002-1670-7364>
 R. Groenewald  <https://orcid.org/0000-0002-5282-7152>
 R. Jaber  <https://orcid.org/0009-0004-7302-5580>
 N. Kafle  <https://orcid.org/0000-0002-8144-787X>
 S. Kamio  <https://orcid.org/0000-0003-0755-2433>
 S. Karbasheski  <https://orcid.org/0000-0003-4988-492X>
 G. Koumariou  <https://orcid.org/0000-0003-0036-4309>
 S. Krause  <https://orcid.org/0009-0004-5525-1218>
 C.K. Lau  <https://orcid.org/0000-0001-6702-1461>
 M. Litton  <https://orcid.org/0000-0002-7617-7473>
 J. MacFarlane  <https://orcid.org/0000-0002-1254-2275>
 D. Marshall  <https://orcid.org/0000-0002-2062-0640>
 R. Mendoza  <https://orcid.org/0000-0002-1761-6165>
 B.S. Nicks  <https://orcid.org/0000-0002-3876-8299>
 S. Ohshima  <https://orcid.org/0000-0003-1341-4969>
 M. Onofri  <https://orcid.org/0000-0003-0818-4628>
 E. Parke  <https://orcid.org/0000-0002-5765-8829>
 S. Patel  <https://orcid.org/0000-0003-3350-9869>
 K. Phung  <https://orcid.org/0000-0002-1732-172X>
 G. Player  <https://orcid.org/0000-0002-2909-5758>
 R.J. Smith  <https://orcid.org/0000-0002-3595-781X>
 V. Sokolov  <https://orcid.org/0000-0003-4971-033X>
 B. Sporer  <https://orcid.org/0000-0001-6290-699X>
 L.C. Steinhauer  <https://orcid.org/0000-0003-2227-7345>
 C. Stonier  <https://orcid.org/0009-0000-4864-4284>
 M. Tobin  <https://orcid.org/0000-0003-2276-6448>
 A.D. Van Drie  <https://orcid.org/0000-0002-6776-9688>
 A. Veksler  <https://orcid.org/0009-0001-4431-4314>
 J. Wood  <https://orcid.org/0009-0004-0670-3628>
 Y. Zhou  <https://orcid.org/0000-0002-8432-3696>

References

- [1] Tuszewski M. 1988 Field reversed configurations *Nucl. Fusion* **28** 2033
- [2] Steinhauer L.C. 2011 Review of field-reversed configurations *Phys. Plasmas* **18** 070501
- [3] Guo H.Y. et al 2015 Achieving a long-lived high-beta plasma state by energetic beam injection *Nat. Commun.* **6** 6897
- [4] Gota H. et al 2021 Overview of C-2W: high temperature, steady-state beam-driven field-reversed configuration plasmas *Nucl. Fusion* **61** 106039
- [5] Rostoker N., Binderbauer M.W. and Monkhorst H.J. 1997 Colliding beam fusion reactor *Science* **278** 1419
- [6] Putvinski S.V., Ryutov D.D. and Yushmanov P.N. 2019 Fusion reactivity of the pB¹¹ plasma revisited *Nucl. Fusion* **59** 076018
- [7] Gota H. et al 2019 Formation of hot, stable, long-lived field-reversed configuration plasmas on the C-2W device *Nucl. Fusion* **59** 112009
- [8] Binderbauer M.W. et al 2010 Dynamic formation of a hot field reversed configuration with improved confinement by supersonic merging of two colliding high- β compact toroids *Phys. Rev. Lett.* **105** 045003
- [9] Binderbauer M.W. et al 2015 A high performance field-reversed configuration *Phys. Plasmas* **22** 056110
- [10] Binderbauer M.W. et al 2016 Recent breakthroughs on C-2U: Norman's legacy *AIP Conf. Proc.* **1721** 030003
- [11] Gota H. et al 2017 Achievement of field-reversed configuration plasma sustainment via 10 MW neutral-beam injection on the C-2U device *Nucl. Fusion* **57** 116021
- [12] Tuszewski M. et al 2012 Field reversed configuration confinement enhancement through edge biasing and neutral beam injection *Phys. Rev. Lett.* **108** 255008
- [13] Schmitz L. et al 2016 Suppressed ion-scale turbulence in a hot high- β plasma *Nat. Commun.* **7** 13860
- [14] Trask E. et al 2016 C-2U experimental transport analysis *Bull. Am. Phys. Soc.* CP10.00064
- [15] Titus J.B. et al 2022 Neutral beam injection on C-2W *Bull. Am. Phys. Soc.* TP11.00029
- [16] Romero J.A. et al 2022 Feedback control of the C-2W field reversed configuration *Bull. Am. Phys. Soc.* TP11.00028
- [17] Romero J.A. et al 2023 Optimization and feedback control of the C-2W field reversed configuration *29th IAEA Fusion Energy Conf. Proc. (London, United Kingdom, 16–21 October)* p IAC/1-1
- [18] Sokolov V. et al 2019 Electrode biasing system in C-2W *Bull. Am. Phys. Soc.* UP10.00141
- [19] Kaur M. et al 2021 Effect of electrode biasing on plasma performance in the C-2W advanced FRC *Int. Workshop on Open Magnetic Systems for Plasma Confinement (OS2021) (Virtual, 24–25 August)*
- [20] Zhai K. et al 2022 C-2W FRC plasma T_e and n_e measurements comparison under different machine configurations *Bull. Am. Phys. Soc.* TP11.00024
- [21] Galeotti L., Barnes D.C., Ceccherini F. and Pegoraro F. 2011 Plasma equilibria with multiple ion species: equations and algorithm *Phys. Plasmas* **18** 082509
- [22] Brul A.V. et al 2021 High-power neutral beam injector with tunable beam energy for plasma heating and stabilization *Plasma Phys. Rep.* **47** 518
- [23] Deichuli P., Davydenko V., Ivanov A., Korepanov S., Mishagin V., Smirnov A., Sorokin A. and Stupishin N. 2015 Low energy, high power hydrogen neutral beam for plasma heating *Rev. Sci. Instrum.* **86** 113509
- [24] Kamio S., Granstedt E.M., Clary R., Player G. and Korepanov S. 2022 Active fast ion charge exchange measurements using a neutral particle analyzer and multiple beam species in C-2W *Rev. Sci. Instrum.* **93** 103516
- [25] Dehaas T. et al 2023 An overview of advancements in the C-2W neutral beam driven field-reversed configuration experiment *Bull. Am. Phys. Soc.* TP11.00108
- [26] Thompson M.C., Schindler T.M., Mendoza R., Gota H., Putvinski S. and Binderbauer M.W. 2018 Integrated diagnostic and data analysis system of the C-2W advanced beam-driven field-reversed configuration plasma experiment *Rev. Sci. Instrum.* **89** 10K114
- [27] Roche T., Romero J., Zhai K., Granstedt E., Gota H., Putvinski S., Smirnov A. and Binderbauer M.W. 2021 The integrated diagnostic suite of the C-2W experimental

- field-reversed configuration device and its applications *Rev. Sci. Instrum.* **92** 033548
- [28] Baltz E.A., Trask E., Binderbauer M., Dikovsky M., Gota H., Mendoza R., Platt J.C. and Riley P.F. 2017 Achievement of sustained net plasma heating in a fusion experiment with the optometrist algorithm *Sci. Rep.* **7** 6425
- [29] Zhai K., Schindler T., Ottaviano A., Zhang H., Fallah D., Wells J., Parke E. and Thompson M.C. 2018 Thomson scattering systems on C-2W field-reversed configuration plasma experiment *Rev. Sci. Instrum.* **89** 10C118
- [30] Gupta S. *et al* 2022 Equilibrium reconstruction of beam driven C-2W plasmas *Bull. Am. Phys. Soc.* TP11.00027
- [31] Brown I.G. 2004 *The Physics and Technology of Ion Sources* 2nd edn (Wiley)
- [32] Titus J.B., Korepanov S., Tkachev A., Pirogov K. and Knapp K. 2021 Wire calorimeter for direct neutral beam power measurements on C-2W *Rev. Sci. Instrum.* **92** 053520
- [33] Titus J.B., Magee R.M., Isakov I., Pirogov K. and Korepanov S. 2018 Secondary electron emission detectors for neutral beam characterization on C-2W *Rev. Sci. Instrum.* **89** 10I123
- [34] Ciric D. *et al* 2011 Performance of upgraded JET neutral beam injectors *Fusion Eng. Des.* **86** 509
- [35] Nations M., Gupta D., Sweeney J., Frausto L. and Tobin M. 2021 Measurements of impurity ion temperature and velocity distributions via active charge-exchange recombination spectroscopy in C-2W *Rev. Sci. Instrum.* **92** 053512
- [36] Gupta D.K., Nations M., Sweeney J., Aviles J., Leinweber H. and Marshall R.S. 2021 Main-ion charge exchange recombination spectroscopy on C-2W FRC plasmas *Rev. Sci. Instrum.* **92** 073508
- [37] Nations M., Romero J.A., Gupta D.K. and Sweeney J. 2022 High-fidelity inference of local impurity profiles in C-2W using Bayesian tomography *Rev. Sci. Instrum.* **93** 113522
- [38] Roche T., Thompson M.C., Griswold M., Knapp K., Koop B., Ottaviano A., Tobin M., Magee R. and Matsumoto T. 2018 Magnetic diagnostic suite of the C-2W field-reversed configuration experiment *Rev. Sci. Instrum.* **89** 10J107
- [39] Tobin M., Roche T. and Matsumoto T. 2021 MHD mode identification by higher order singular value decomposition of C-2W Mirnov probe data *Rev. Sci. Instrum.* **92** 043510
- [40] Granstedt E.M., Gupta D., Sweeney J., Tobin M. and Dikovsky M. 2021 Comprehensive imaging of C-2W plasmas: instruments and applications *Rev. Sci. Instrum.* **92** 043515